JOURNAL OF MATERIALS SCIENCE 33 (1998) 1661–1675

Processing, microstructure and fracture behaviour of a spray-atomized and deposited nickel aluminide intermetallic

D. LAWRYNOWICZ, X. LIANG, T. S. SRIVATSAN*, E. J. LAVERNIA
Department of Chemical Engineering and Materials Science, University of California, Irvine, CA 92717, USA
** Department of Mechanical Engineering, The University of Akron, Akron, OH 44325-3903, USA*

In this study, nickel aluminide intermetallics were synthesized using the spray atomization and deposition technique. Microstructure characterization studies were performed to provide an understanding of the intrinsic influence of spray processing parameters on the microstructure of the intermetallic. Numerical simulation was carried out to provide an understanding of the influence of deformation, heat transfer kinetics and thermal history of the droplets on the thermal profile, distribution and solidification. The microstructure of the intermetallic is discussed in the light of results obtained from experimental observations and numerical simulation. Ambient-temperature tensile tests reveal the intermetallics to have a high strength and acceptable ductility. The tensile fracture behaviour of the polycrystalline intermetallic is presented and discussed in the light of processing and thermal conditions during spray deposition and intrinsic microstructural effects. © *1998 Chapman & Hall*

Nomenclature

a_l, a_s	thermal diffusivities of liquid and solid, respectively
A_s	area of substrate surface
b	thickness of molten metal
c_l, c_s	heat capacities of liquid and solid, respectively
C_{pm}	specific heat of metal
D	initial impact droplet diameter
E_k	kinetic energy
E_p	potential energy (due to surface tension)
f	fraction solidified
f_{ave}	average solid fraction in droplet
F	volume fraction of void
$\boldsymbol{F}_b$	body force vector
g, $\boldsymbol{g}$	gravitational acceleration and gravitational acceleration vector, respectively
Δh	enthalpy of fusion
h_{bot}	heat transfer coefficient at the interface between the deposit and the substrate
h_{top}	heat transfer coefficient; convective heat exchange between the atmosphere and the top surface of the deposit
H	thermal enthalpy of deposited material
J_m	mass flow rate of metal
K_l, K_s	thermal conductivities of liquid and solid, respectively
K_m	thermal conductivity of metal
L_f	work of the frictional forces
p	scalar pressure
Pe	$\omega D/a_s$, Peclet number
r	radial coordinate
Re	$\rho_l D\omega/\mu$, Reynolds number
$R(t^*)$	radius of the solidified disc
t	time
T_0, T_p	dimensionless temperatures of substrate and droplet, respectively
T_l, T_m, T_s	droplet temperature, melting temperature and substrate temperature, respectively
u	transformation temperature defined in [38]
U	freezing constant
v	radial velocity of droplet
$\boldsymbol{v}$	velocity vector
We	$D\omega^2\rho_l/\sigma$, Weber number
X	thickness of spray-deposited material
X_f	final height of deposit
Y	thickness of the solidified layer at any real time t after impact
z	axial coordinate
ε	constant ($=0.5$)
ρ_l, ρ_s	densities of liquid and solid, respectively
μ	coefficient of dynamic viscosity
σ	surface tension coefficient
Θ	volume fraction of liquid

1. Introduction

Major advances in technology, coupled with an increasing need for light-weight high-strength high-performance structural materials which can be used at

temperatures higher than those currently possible with conventional titanium and nickel-based alloys, have engendered considerable scientific and technological interest in the development of a new generation of structural materials. Ordered intermetallic alloys constitute a unique class of metallic materials that are attractive alternatives to the conventional nickel-based superalloys. These compounds have been recognized for their superior elevated-temperature strength, superior creep resistance, fatigue and damage tolerance, corrosion resistance, low density and high thrust-to-weight ratio [1, 2]. The chemical ordering in these intermetallic compounds reduces atom mobility at elevated temperatures, resulting in improved structural stability and resistance to high-temperature deformation [1]. The ordered intermetallic compounds of nickel and aluminium (NiAl and Ni_3Al) have in recent years been the subject of intense research activity because of the excellent resistance to oxidation, high melting temperatures and relatively low density. These characteristics make them attractive candidates for potential use as engine materials for future military aircraft and supersonic commercial transport aircraft such as the National Aerospace Plane and the high-speed civil transport aircraft [3–6]. The strong bonding between aluminium and nickel, which persists at elevated temperatures, provides high strength such that the specific strengths of the intermetallic materials are competitive with those of the superalloys and even ceramics [3].

Alloys based on the nickel aluminide intermetallic, Ni_3Al, have an $L1_2$ (ordered face-centred cubic (f.c.c.)) crystal structure and is perhaps best known as the gamma prime (γ') strengthening phase in some nickel-based superalloys. The Ni_3Al intermetallic has been considered for a spectrum of applications such as gas turbines and stream turbines, and components used in corrosive environments (oil and gas wells, and chemical process industry) [5, 6]. The Ni_3Al intermetallic compound is of interest for use at elevated temperatures primarily because its yield strength actually increases with an increase in temperature up to 750 °C [3, 7]. Besides unusual strength behaviour, good creep characteristics, oxidation and corrosion resistance have also been identified with this nickel aluminide intermetallic compound. However, extensive use of the Ni_3Al intermetallic, in polycrystalline form, as an engineering material is rendered difficult on account of its limited ductility, poor-fracture-related properties at ambient temperature and limited fabricability [8–11]. The inferior ductility and tendency for brittle behaviour was a major obstacle that placed constraints on the development and use of polycrystalline Ni_3Al alloys and precluded their use for structural components because of lack of fabricability and fear of premature catastrophic failure.

The inferior ductility of the intermetallic compound was attributed to the concurrent and mutually interactive influences of [12–16] the following:

(a) a low cohesive strength of grain boundaries;
(b) embrittling effects of impurities at the grain boundaries;
(c) an insufficient number of slip systems to satisfy von Mises criterion for general plasticity of a polycrystalline material;
(d) a tendency to fail in a brittle intergranular fracture mode;
(e) a low initial density of mobile dislocations.

In recent years, alloy design efforts have focused on compositional modifications as a means of improving the ductility, fracture-related properties and fabricability of Ni_3Al-based alloys. The effects of small additions of boron to the Ni_3Al intermetallic have been studied by several groups of investigators [17–23]. Interest in the use of boron as a microalloying addition was triggered by an appreciable improvement in ductility of polycrystalline nickel aluminide alloys due to a change in fracture mode from brittle intergranular to predominantly ductile transgranular fracture in smooth tensile specimens [24]. Boron segregates strongly to linear and planar defects including small- and large-angle grain boundaries, twin boundaries and antiphase boundaries, stacking faults, and dislocations [25, 26]. The strengthening effect of boron additions was attributed to concurrent and mutually interactive influences of firstly improvements in grain-boundary cohesive strength, secondly increased disordering at grain boundaries caused by boron segregation and thirdly enhanced plastic flow in the grain-boundary regions.

The rationale for the present study was to provide an insight into microstructural evolution and fracture behaviour of spray-atomized and deposited Ni_3Al. Evolution of the microstructure of the intermetallic is discussed in the light of the results obtained from experimental studies, microstructural observations and numerical simulation. The quasistatic fracture behaviour of the polycrystalline intermetallic is discussed in terms of processing and intrinsic microstructural effects.

2. Spray atomization and deposition

Over the past decade, spray atomization and deposition have attracted considerable attention as a viable processing alternative for structural materials and have been applied successfully to numerous alloy systems [27–31]. This synthesis methodology essentially refers to a two-step process route.

(a) The molten metal disintegrates energetically, by an inert gas, into micron-sized droplets (atomization).
(b) Subsequently a mixture of solid, liquid and partially solidified droplets is deposited on a substrate surface [32]. The droplets eventually collect as a coherent preform, the microstructure of which is dictated largely by the solidification conditions of the droplets during impact. This synthesis methodology offers a potentially attractive manufacturing route for the following reasons.

1. The highly efficient heat extraction during atomization ensures the maintenance of processing temperatures that are lower than those corresponding to

casting processes; this limits large-scale segregation and associated coarsening phenomena.

2. The inert conditions required for atomization and deposition minimize surface oxidation and other deleterious surface reactions.

3. Spray atomization and deposition can potentially be used for near-net-shape manufacturing of difficult to form materials, such as the ordered intermetallic compounds and discontinuously reinforced metal-matrix composites [33–35].

A detailed study of the solidification mechanisms that govern the evolution of microstructure during spray atomization and deposition is rendered complex by the extreme differences in thermal environment both before and after impact of the droplets with the deposition surface. During atomization, the violent and/or rapid extraction of thermal energy by the atomization gas promotes the formation of highly refined microstructures [36]. In contrast, the solidification conditions after the distribution of droplets strikes or arrives at the deposition surface are governed by relatively sluggish cooling rates (10–100 °C s^{-1}) [37, 38]. The microstructure of spray-atomized and deposited materials is generally reported to exhibit spheroidal or "equiaxed" grains, a feature that is consistently observed regardless of alloy composition [39, 40]. Recently, a comprehensive study of the phenomena has been reported and discussed in detail [41]. Furthermore, recent work on the interfacial behaviour in metal-matrix composites processed by spray atomization and deposition has revealed some interesting insights into the thermal and solidification conditions that govern microstructural evolution [42–44].

3. Experimental procedure

The alloys used in this study were provided by Oak Ridge National Laboratory (Oak Ridge, TN, USA) and were designated as IC-50 and IC-396. The nominal chemical compositions of the as-cast IC-50 and IC-396 Ni_3Al are summarized in Table I. Zirconium additions aid in improving high-temperature strength through solid-solution-strengthening effects, while controlled microalloying with boron enhances grain-boundary cohesive strength and helps to improve ductility at ambient temperature [45, 46]. Addition of chromium and molybdenum promotes the formation of protective oxide films that either enhance or improve the oxidation resistance at elevated temperatures.

The synthesis of Ni_3Al by spray atomization and deposition, henceforth referred to in the manuscript as spray deposition, involves the following procedure. Both the Ni_3Al intermetallic alloys were superheated to 1823 K and disintegrated into a fine distribution of micron-sized droplets using nitrogen gas and an atomization pressure of 2.41 MPa. The mass flow rates of the atomization gas and metal were 0.078 kg s^{-1} and 0.022 kg s^{-1}, respectively. To avoid oxidation of the Ni_3Al intermetallic during spray deposition processing, the experiments were conducted inside an environmental chamber which was evacuated down to a pressure of 200 Pa and back filled with nitrogen to a pressure of 101 kPa prior to melting and atomization. Following atomization, the partially solidified Ni_3Al droplets were deposited onto a water-cooled substrate positioned at a distance of 25.4 cm from the atomization nozzle. The droplets eventually collect as a coherent preform. The spray atomization and deposition apparatus used in this study is shown in Fig. 1. In addition to the material deposited on the substrate, the over-spray-atomized powders were collected in a cyclone separator. The size distribution of these powders was established from sieve experiments in accordance with ASTM Standard B:214 [47] and MPIF Standard 5.

TABLE I Nominal chemical composition of the nickel aluminide (Ni_3Al) intermetallics

Alloy	Amount (at. %)					
	Al	B	Cr	Mo	Zr	Ni
IC-50	21.8	0.09	—	—	0.30	Balance
IC-396	16.3	0.03	8.10	1.7	0.50	Balance

In order to characterize experimentally the thermal history of the material during processing, the temperature inside the deposit was measured by placing a type C (tungsten–5% rhenium versus tungsten–26% rhenium; temperature range, 273–2593 K; lag time, 0.9 s) thermocouple at a location which was 10 mm from the substrate surface. Samples from both the over-spray powders and the spray-deposited materials were prepared for microstructural analysis using standard metallographic techniques. Marble's reagent (10 g of $CuSO_4$ + 50 ml of HCl + 50 ml of H_2O) was used to etch polished cross-sections of the samples. The microstructural characteristics were examined quantitatively using an ImageSet image analysis system developed by Dapple Systems Incorporated. This procedure permitted an efficient analysis of a large number of samples. Tensile test samples, conforming to the geometry and dimensions in Fig. 2, were precision machined from the as-deposited alloys. Uniaxial tensile tests were performed on a fully automated closed-loop servohydraulic MTS 810 test machine equipped with a 100 kN load cell. The specimens were deformed to failure at a constant strain rate of 1×10^3 s^{-1}. The tests were performed in controlled laboratory air environment (relative humidity, 60%; ambient temperature, 298 K). Samples for scanning electron microscopy (SEM) observation were obtained from the fractured tensile samples by sectioning parallel to the fracture surface. Fracture surfaces of the deformed tensile samples were examined in a scanning electron microscope firstly to determine the macroscopic fracture mode, and secondly to characterize the fine-scale topography and microscopic mechanisms governing quasistatic fracture. The distinction between macroscopic mode and microscopic fracture mechanisms is based on the magnification level at which observations are made. The macroscopic mode

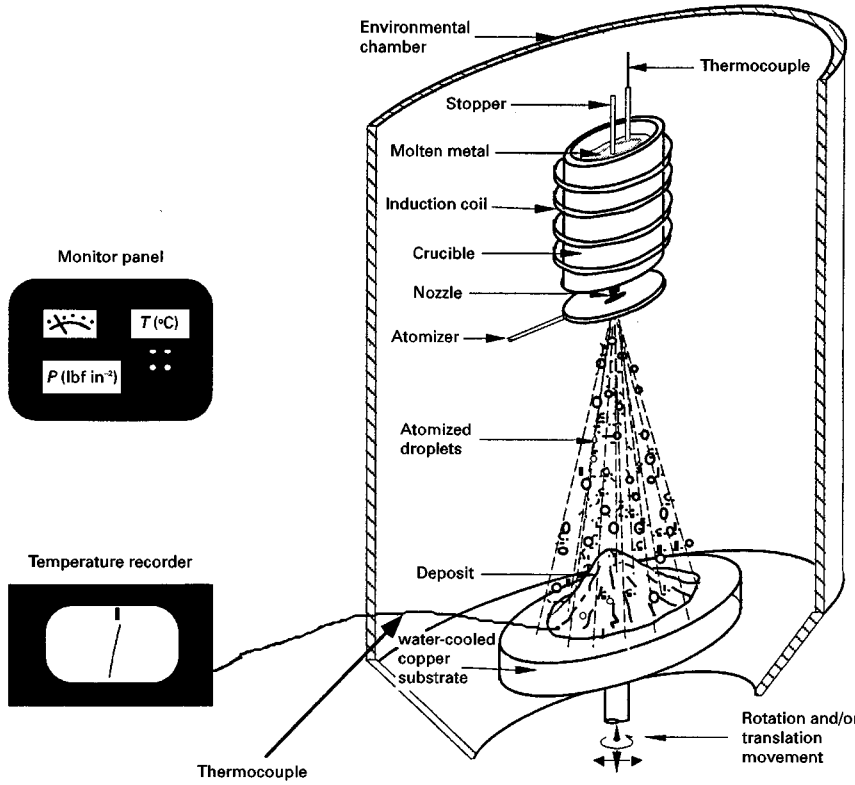

Figure 1 Schematic diagram showing the experimental apparatus used for spray atomization and deposition processing.

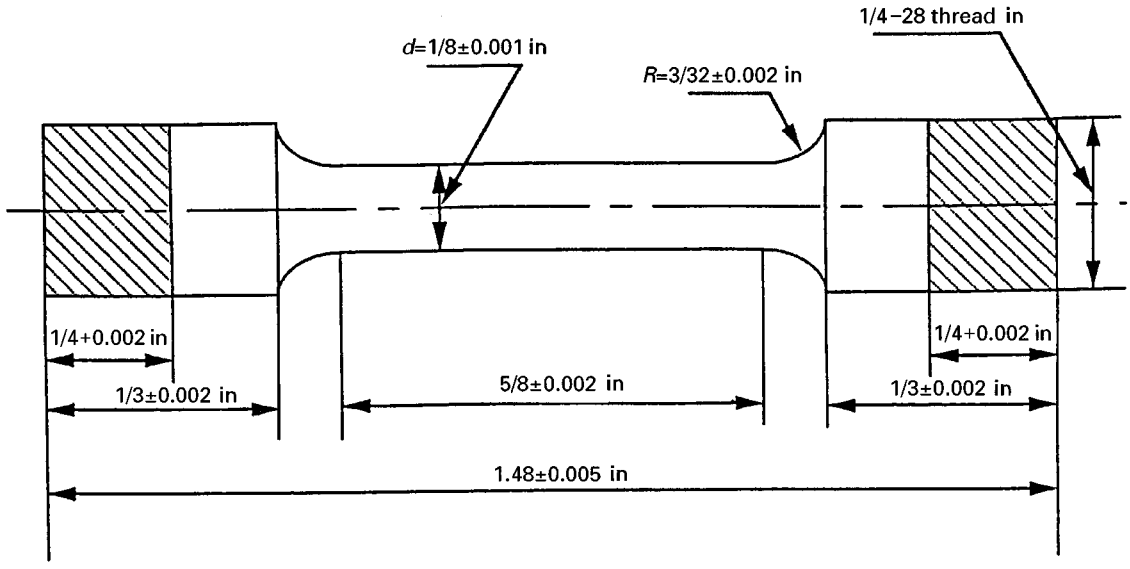

Figure 2 Tensile test specimen geometry and dimensions for both the IC-50 and the IC-396 alloys.

refers to the nature of failure while the microscopic mechanism relates to the local failure processes (microvoid formation, coalescence and intergranular cracking). Additionally, transmission electron microscopy (TEM) was utilized to gain further insight into the grain-boundary structure and operative dislocation mechanisms in the fractured Ni_3Al specimens. Furthermore, X-ray diffraction (XRD) was performed to verify the phase composition and presence of the long-range ordered $L1_2$ structure in the Ni_3Al intermetallic materials.

4. Results and discussion

4.1. Microstructure and cooling rate in as-deposited materials

Systematic microstructural characterization studies have been conducted on the spray-atomized and deposited Ni_3Al intermetallics (IC-50 and IC-396). XRD characterization results shown in Fig. 3 reveal both materials to exhibit an identical crystal structure ($L1_2$) which is consistent with the ordered Ni_3Al powder diffraction file standard (PDIF 9-97). Additionally TEM convergent-beam diffraction (CBD) patterns

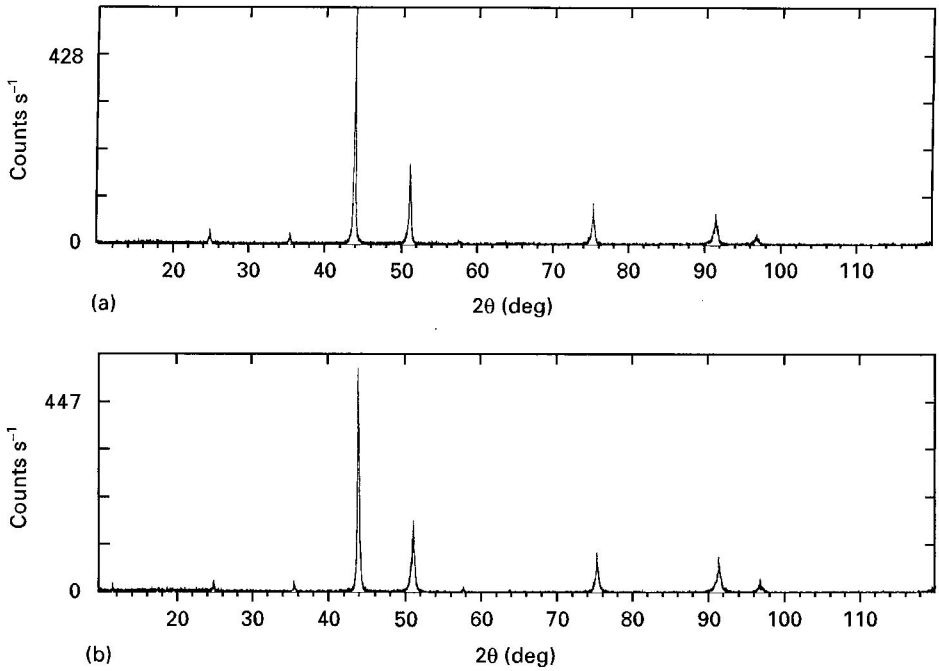

Figure 3 XRD results for (a) IC-50 and (b) IC-396 (all peaks shown match Ni_3Al PDIF 9-97).

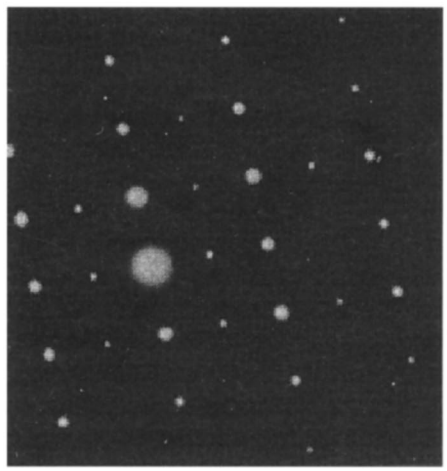

Figure 4 CBD pattern for the Ni_3Al intermetallics showing the primary f.c.c. [110] zone-axis reflections (strong) and the superlattice reflections (weak) for the ordered $L1_2$ structure.

confirmed this result (Fig. 4) by revealing the superlattice structure found in both the IC-50 and the IC-396 alloys. The conspicuous absence of any diffraction peaks corresponding to the various microalloying constituents is expected because of their relatively small content and/or fine distribution within the materials, which makes it extremely difficult to detect. Furthermore, the materials were analysed with particular emphasis on the precise geometric location of the microstructural features of interest [41]. In view of the TEM and XRD results as well as similar processing parameters it was not surprising to find that both intermetallics exhibited nearly identical microstructural features. At and near the substrate, the microstructure of the two intermetallic materials (IC-50 and IC-396) consisted of densely packed powders that deformed upon impact with the substrate forming thick prior-droplet boundaries between them

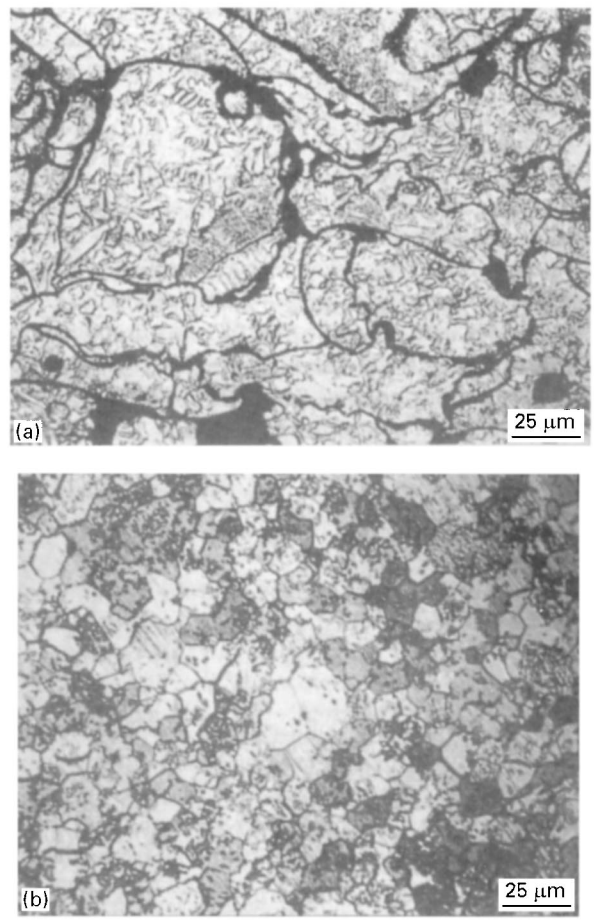

Figure 5 Optical micrographs of IC-50: (a) layered microstructure of deformed, fractured dendrites and thick prior-droplet boundaries located near the substrate; (b) microstructure showing fine spheroidal grains representative of the interior of the deposit.

(Fig. 5a). This gave the region a highly irregular appearance. At the local level, the microstructure within the deformed powders consisted of a mixture of the

following:

(a) deformed dendrite arms;
(b) fractured dendrite arms;
(c) dendrite arms aligned perpendicular to the deposition surface.

In general, microstructural observations of the material in this region suggest that the droplets were partially solidified during impact with the deposition surface. It is interesting and noteworthy to observe that most of the dendrites that were examined in the substrate region appeared to have experienced either extensive plasticity or fracture.

Modelling of the deformation and solidification of a single molten metal droplet impinging onto a flat surface provides some insight into the reason why microstructure evolution varies with location within the deposited material [48–58]. Spray atomized droplets are typically found to form very thin discs during solidification upon a flat substrate. Fig. 6a shows a computer modelled history of a single liquid metal droplet impinging on a flat surface [48]. The thickness of the droplet splat and the resulting morphology may be inferred from the mathematical modelling of this phenomenon originally proposed by Madejski [49].

Conceptually, the model that Madejski formulated was based on an energy balance for the motion of the liquid metal droplet after impact with the substrate. Three components, namely, E_k (the kinetic energy), E_p (the potential energy due to surface tension) and L_f (the work of the frictional forces) governed the entire process. Conservation of energy dictated that the total energy must be constant with time; consequently

$$\frac{d}{dt^*}(E_k + E_p + L_f) = 0 \tag{1}$$

Furthermore, study of the energy forces involved in the deformation process lead Madejski to formulate the following relationships for the three energy components:

$$E_k = \frac{\pi}{3}\rho_1\left(\frac{dR}{dt^*}\right)^2(bR^2 + \tfrac{6}{5}b^3) \tag{2}$$

$$E_p = \delta(\pi R^2 + 2\pi Rb) \tag{3}$$

$$L_f = \int_0^{t^*} \frac{\pi R^2 \mu}{b}\left(\frac{dR}{dt^*}\right)^2 dt^* \tag{4}$$

where ρ_1 is the density of the liquid, $R(t^*)$ is the radius of the solidified disc, δ is the surface tension of the liquid and μ is the viscosity of the liquid.

Incorporating mathematical relationships for the Peclet, Reynolds and Weber numbers reveals that

$$Pe = \frac{\omega D}{a_s} \tag{5}$$

$$Re = \frac{\rho_1 \omega D}{\mu} \tag{6}$$

$$We = \frac{\rho_1 \omega^2 D}{\delta} \tag{7}$$

where ω is the velocity of the liquid droplet at impact, a_s is the thermal diffusivity of the solid layer and D is the diameter of the original spherical droplet. Furthermore, the relationships for the temperature, T_0, of the substrate and temperature, T_p, of the droplet have been shown to be

$$T_0 = \frac{K_s(T_m - T_s)}{a_s \rho_s \Delta h} \tag{8}$$

$$T_p = \frac{K_s(T_l - T_m)}{a_s \rho_s \Delta h} \tag{9}$$

where K_s is the thermal conductivity of the solid, T_m, T_s and T_l are the melting temperature, the substrate temperature and the liquid temperature, respectively, and Δh is the enthalpy of fusion. Madejski was able, through numerical methods and many intermediate

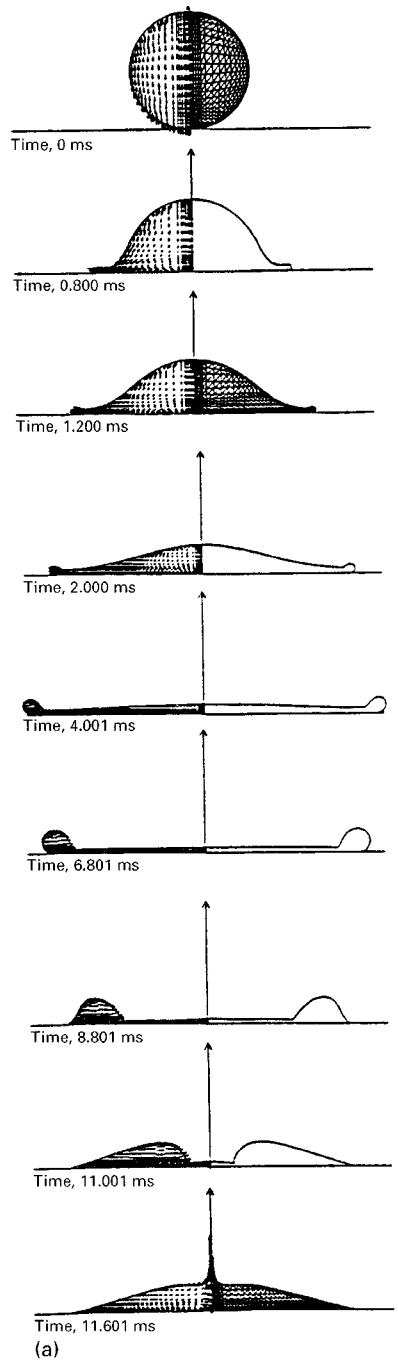

Figure 6 (a) Computer modelled history of a liquid metal droplet impacting a flat surface.

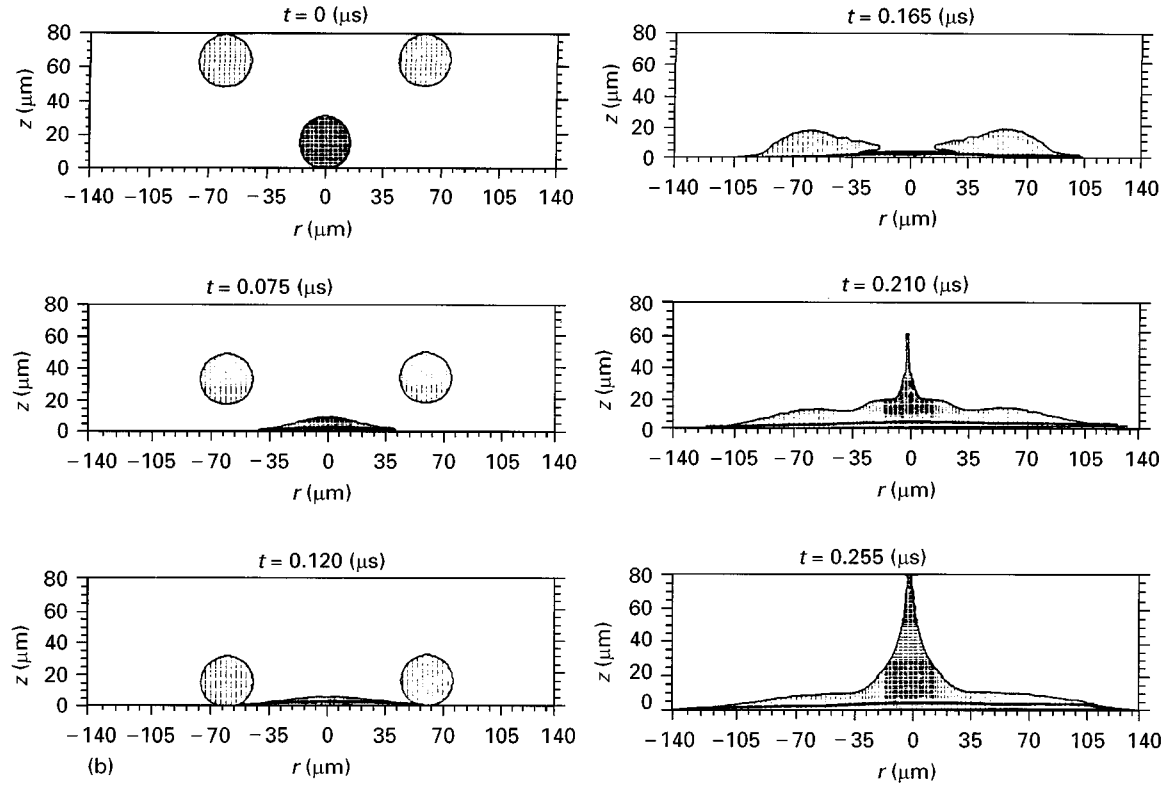

Figure 6 (b) Deformation and solidification sequence of several droplets (D = 30 μm).

equations (see [49] for a more detailed account of the numerical analysis) to model the history of deformation and solidification of a single droplet of molten metal.

Deformation and solidification of a single droplet provide a rudimentary basis for understanding some of the events which occur during deposition. Utilizing some of the concepts and presumptions of this work as a foundation allows for the formulation of models incorporating the deposition of many droplets which will be discussed in the following section. However, even though single-droplet modelling is not realistically useful except for understanding the processes at work, it does elucidate how velocity, droplet size, surface tension and density affect the final microstructure of spray deposits.

In real systems involving the accumulation of many solidifying droplets, other factors must be considered. Specifically, in practical systems, the droplets accumulate into a deposit having an irregular surface. Other modelling studies have shown [50] that droplets may break apart into smaller splats upon impact with irregular features and additionally the thickness of the splats will be larger than that predicted for the single-droplet flat-substrate model owing to the irregular geometry. Investigations performed by Liu *et al.* [51–54] elaborated on the numerical work of Madejski and incorporated the modelling of interaction of several droplets impinging on one another and a flat surface as well as the premise that some solid fraction is present within the droplets prior to impact. Using some simplifying assumptions and the full Navier–Stokes equation for transient axisymmetric viscous incompressible fluid flow, and the transport equation for the volume-of-fluid (VOF) function, Liu *et al.* were able to determine the exact movement and interaction of droplets in a two-dimensional domain. Modifying Madejski's model to incorporate solidification during droplet deformation provided a more realistic modelling of the atomization phenomena and consisted of the following governing equations modified on the basis of a two-phase flow continuum model:

$$\nabla\cdot(\Theta \boldsymbol{v}) = 0 \tag{10}$$

for continuity

$$\Theta\frac{\partial \boldsymbol{v}}{\partial t} + \nabla\cdot(\Theta \boldsymbol{v}\boldsymbol{v}) = -\frac{\Theta}{\rho}\nabla p + \frac{\Theta}{\rho}\nabla\cdot\boldsymbol{\tau} + \Theta \boldsymbol{g} + \Theta \boldsymbol{F}_{\mathrm{b}} \tag{11}$$

for the momentum transport, and

$$\frac{\partial}{\partial t}(\Theta F) + \nabla\cdot(\Theta F v) = 0 \tag{12}$$

for VOF transport (the variables used are described in the nomenclature). In the flow problem involving a growing solid layer, the solidified part is simulated with a two-phase flow continuum model developed by Liu *et al.* [51–54]. In this continuum model, the flow is modelled as a special case of two-phase flow by introducing a volume fraction Θ, which is a continuous average quantity defined to be unity at any point occupied by fluid, zero at any point occupied by solid, and between zero and unity at the solid–liquid

interface:

$\Theta = 1$ fluid cell

$0 \leqslant \Theta \leqslant 1$ interface

$\Theta = 0$ solid cell

Working on the premise that the heat diffusion and solidification process within a splat may be simplified into one dimension on the basis of the splat solidification mechanisms [59] where the predominant heat extraction is in the direction from the splat to the substrate, Liu *et al.* estimated the thickness of the solidified layer in the splat using the one-dimensional solution of the Stefan problem of solidification given by [49, 50, 55]

$$Y = U[a_s(t - t_i)]^{1/2} \quad (13)$$

with the freezing constant U [49, 50, 55]

$$U = \frac{2}{\pi^{1/2}} \left(\frac{T_0}{\text{erf}(U/2)\exp(U^4/4)} - \frac{T_p(K_l c_l \rho_l / K_s c_s \rho_s)^{1/2}}{\text{erfc}[(U/2)(a_s/a_l)^{1/2}]\exp(-U^2 a_s/4a_l)} \right) \quad (14)$$

where T_0 and T_p are defined previously by Equations 8 and 9. The results of the modelling efforts of Liu *et al.* are displayed in Fig. 6b, where the solidification and deformation sequence of several droplets is presented. From the computer modelling of Fig. 6b it is evident how complex the spray atomization and deposition process can be with the inclusion of millions of droplets. In this microcosm environment with three droplets it can be seen how the droplet which impinges a smooth surface tends to flatten out, consistent with Madejski's [49] model, while subsequent droplets experience complex interactions resulting in a diversified morphology as evident in the microstructural gradient from the bottom to the top of the deposit as discussed in the subsequent section of this investigation. As a result, from incorporation of the experimental results as well as the modelling, it becomes apparent that factors such as initial droplet size, droplet velocity and material properties of the droplet ultimately dictate the final morphology of the deposit.

The deformation theory of the droplets and the observed microstructures suggest that the mechanical deformation of the semisolid droplets resulting from the individual droplets impacting the substrate can cause separation of the dendrites preferentially along dendrite boundaries. The droplets impacting at or near the chilled substrate experience extremely high heat extraction rates, causing the preservation of the fragmented, deformed dendrite arms structure to be preserved when the liquid portion of the impacting droplet solidifies and preferentially forms dendrite arms aligned perpendicular to the deposition surface as a result of the direction of the maximum heat extraction gradient. This deformation and solidification scenario may explain the microstructure observed in the deposit near the substrate.

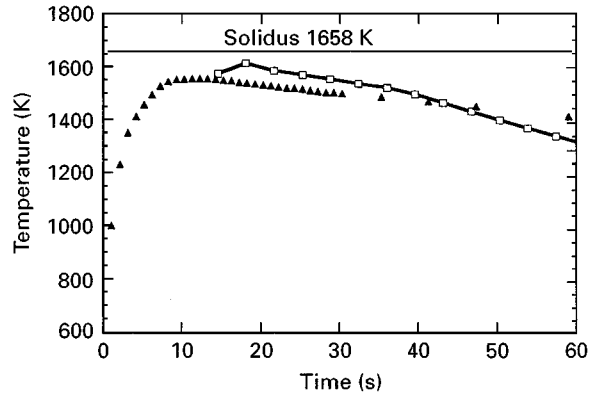

Figure 7 Measured (▲) and calculated (—□—) temperature profile in spray-deposited Ni_3Al at a location 10 mm from the substrate.

A large fraction of the microstructure of the two spray-deposited intermetallics consisted of fine, homogeneous and fully spheroidal grains, with an average size of 10 μm. The microstructure appeared to be reasonably dense (Fig. 5b), with a porosity of only 1.3% as measured by the image analysis technique [60]. This correlates well with the numerical modelling which predicts that the kinetic energy, associated with the moderate density (6.81 g cm^{-3}) of Ni_3Al, and atomization with high-velocity (520 m s^{-1}) gas, readily overcomes the surface tension energy of the droplets spreading or flattening the droplets upon impact into thin wide discs which are readily stacked in a dense efficient manner, thereby limiting porosity. The microstructure of the spray-deposited material in regions away from the substrate consisted of a mixture of the intrinsic features associated with the two previously described regions. The near-spheroidal grains present in regions away from the substrate were not fully developed and their distribution was heterogeneous. Prior-droplet boundaries were readily seen in this region, although they were thinner than those present at and near the substrate.

During spray atomization and deposition, the temperature at a location 10 mm above the substrate surface (on the spray axis), inside the deposited material, was concurrently measured and recorded in order to study the thermal profile and/or history during processing. The results are exemplified in Fig. 7 and presented together with the solidus temperature of the Ni_3Al intermetallic used in the present study. The measured temperature profile reveals the temperature at this location in the deposited material to be below the solidus temperature. In addition, an average cooling rate for $T > 0.5T_m$ was measured to be approximately 2.6 K s^{-1} on the basis of the measured temperature profile.

The ambient temperature tensile properties are summarized in Table II. Results reveal alloy IC-396 to have better yield strength and ultimate tensile strength than the intermetallic IC-50. The improvement is far more noticeable in the yield strength than in the ultimate tensile strength. The improved strength resulted in a 20% degradation in room temperature tensile ductility of the IC-396 over the IC-50 counterpart.

TABLE II Tensile properties of nickel aluminide (Ni_3Al) intermetallics, where the results are the mean values based on duplicate tests

Alloy	Offset yield strength (MPa (klbf in^{-2}))	Tensile strength (MPa (klbf in^{-2}))	Elongation, ε, in 25 mm (%)
IC-50	441 (64)	974 (141)	22.0
IC-396	788 (114)	1085 (157)	18.0

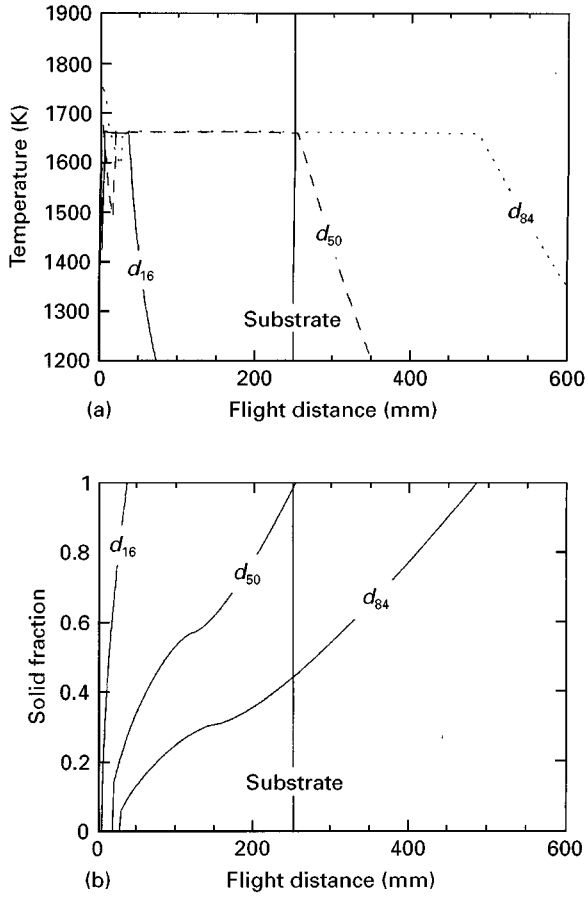

Figure 8 (a) Calculated temperature profiles of Ni_3Al droplets during atomization. (b) Calculated solid fraction of Ni_3Al droplets during atomization.

4.2. Thermal profile in the spray-deposited materials

As shown in Fig. 8, droplets arriving on the deposition surface are either in the fully solid, fully liquid or partially solid condition. Moreover, the fine dendritic microstructures that are present in the powders provide experimental support for the relatively fast rates of heat extraction that were computed on the basis of athermal considerations. However, it is evident that there will be intrinsic microstructural variations within a single droplet, in both scale and morphology, owing to the complex thermal history experienced by the droplet, namely undercooling, nucleation, recalescence and equilibrium solidification. Thus, a highly heterogeneous mixture of microstructures arrives on the deposition surface and eventually collects as a highly dense preform. The microstructure of the preform is dependent critically on the concurrent and mutually competitive influences of solidification characteristics of the impinging droplets and ensuing interactions with each other and with the deposition surface.

In view of the fact that the thickness of the spray-deposited material is several orders of magnitude larger than that of a single droplet, the thermal gradients that exist during deposition must be determined. The instantaneous average thickness of the spray-deposited material, say X, may be readily calculated on the basis of a mass balance [38]:

$$X = \frac{J_m}{\rho_s A_s} t \tag{15}$$

where J_m is the mass flow rate of metal, ρ_s is the density of the metal and A_s is the area of the substrate surface. The temperature distribution in the growing deposit may be calculated from the differential thermal energy balance equation, assuming that heat conduction takes place only in a direction perpendicular to the deposition surface (defined as the x direction). This appears to be a reasonable assumption considering that both the water-cooled copper substrate and the atomizing gas are the primary sources of heat extraction during deposition. The one-dimensional thermal energy equation may be expressed as:

$$\frac{\partial H}{\partial t} = \frac{\partial}{\partial x}\left(\frac{\partial u}{\partial x}\right) \tag{16}$$

where H is the thermal enthalpy of the deposited material and U is the transformation temperature defined and described in detail elsewhere [38]. The heat transfer process that occurs within the deposited material is subject to the following initial and boundary conditions.

(a) During the initial stages, the total thermal energy of the distribution of droplets, impinging first on the deposition surface and eventually with each other, may be estimated by considering the fraction solidified present in each droplet at the time of deposition onto the water-cooled substrate. This assumes no change in droplet size with respect to flight distance. On the basis of observed experimental results (Fig. 9) the size distribution of the droplets may be represented by a logarithmic-normal relationship. Therefore, the average thermal condition of droplets may be estimated from three diameters that characterize the distribution of droplet sizes, namely, d_{16}, d_{50} and d_{84}. On the basis of logarithmic-normal statistics, it follows that d_{16} and d_{84} each represent 32% while d_{50} represents 36% of the total mass of the droplets arriving on the substrate, as shown in Fig. 10a. Then, the average fraction solidified is calculated from the expression

$$f_{ave} = (f_{16} + f_{84}) \times 32\% + f_{50} \times 36\% \tag{17}$$

where f_{16}, f_{50} and f_{84} are the solidified fraction of the droplets of size d_{16}, d_{50} and d_{84}, respectively. The

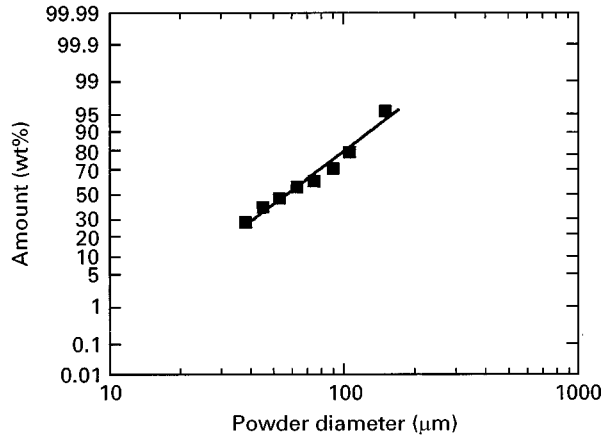

Figure 9 Powder size distribution of atomized Ni_3Al powders determined from sieving experiments.

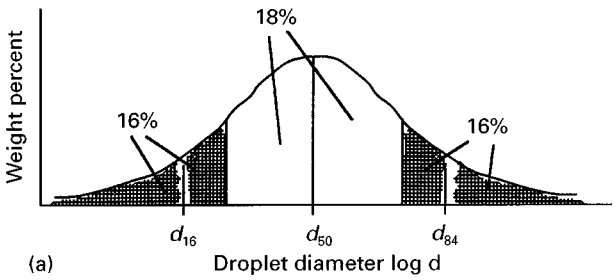

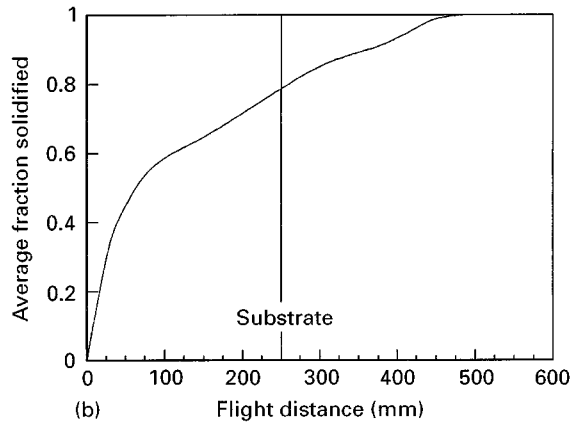

Figure 10 (a) Schematic diagram showing calculation of the average volume fraction solidified. (b) Calculated average volume fraction solidified f_{ave} as a function of flight distance for the conditions used in the present study.

results calculated on the basis of Equation 17, taking into consideration the fraction solidified for each droplet diameter as summarized in Fig. 8b, are shown in Fig. 10b. The results reveal that the average fraction solidified initially increases rapidly with increasing flight distance and eventually approaches a quasi-steady-state behaviour until complete solidification is achieved. The results also reveal that the average solidified fraction of the impinging spray corresponds to approximately 75%.

(b) At the deposition preform surface, i.e. at $x = 0$, the temperature satisfies the relationship

$$K_m \frac{\partial T}{\partial x} = h_{bot}(T - T_s) \quad (18)$$

where K_m is the thermal conductivity of the metal, h_{bot} is the heat transfer coefficient at the interface between the deposit and the substrate and T_s is the temperature of the substrate.

(c) At the top of the deposit, i.e. at $x = X$, the temperature obeys the equation

$$K_m \frac{\partial T}{\partial x} = H_d \frac{J_m}{A_s} - h_{top}(T - T_0) - \varepsilon\sigma(T^4 - T_0^4) \quad (19)$$

where the heat transfer coefficient, h_{top}, for the convective heat exchange between the atmosphere and the top surface of the deposit is assumed to be at least an order of magnitude smaller than h_{bot}, and T_0 is the temperature of the gas. This appears to be a reasonable assumption on the basis of experimental findings of Annavarapu *et al.* [59]. It should be noted that the first term on the right-hand side of Equation 19 represents the heat (determined by the average solid fraction) input from the impinging spray to the preform and effectively becomes zero once deposition is complete.

Using the values of initial and boundary conditions, as listed in Table III, the thermal history experienced by the spray-deposited material may be calculated using Equations 16–19. The results are shown in Fig. 7 for a point positioned 10 mm above the substrate–deposit interface inside the spray-deposited material. In this figure, the calculated temperature profile is compared with results obtained experimentally. The relatively good agreement between the calculated and measured temperature profiles provides support to the model formulation. Furthermore, it is also evident from the results that the temperature of the material during spray deposition remained below the solidus temperature of the material, despite the fact that the distribution of droplets contained a finite amount of volume fraction of liquid.

On the basis of the aforementioned discussion, the different intrinsic microstructural features present in the two spray-deposited intermetallics are summarized as follows. The microstructure present at the exterior, namely the bottom area of the deposit (Fig. 5a), is dominated by the presence of fine powders that arrived on the substrate in the fully solidified condition and were embedded in the minority of the droplets, already on the substrate, that contained finite amounts of liquid. Recent studies on the measurement of droplet sizes during atomization, using Doppler techniques [60], have shown that the peripheral region of the atomized spray is populated by droplets that are substantially smaller than those present in the centre of the spray. Also, the droplet mass flux decreases with increasing distance from the spray axis. Consequently, as supported by numerical results obtained (see Fig. 8), small droplets in this region arrive on the substrate fully solidified and were enveloped by larger droplets which contained some liquid. The extremely high heat extraction rate associated with the area adjacent to the substrate "freezes" the small fully solidified droplets inside the larger droplets containing the fragmented dendrites resulting

TABLE III Physical constants and parameters used in calculating the thermal history of droplets during deposition (the properties of IC-50 and IC-396 are based entirely on Ni_3Al, not including any alloying constituents)

Parameter	Description	Value
J_m	Liquid metal mass flow rate	0.078 $kg\,s^{-1}$
A_s	Area of substrate surface	0.0153 m^2
X_f	Final height of deposit	0.026 m
h_{bot}	Heat transfer coefficient of deposit–substrate	550.0 $W\,m^{-1}\,K^{-1}$
h_{top}	Heat transfer coefficient of deposit–gas	21.0 $W\,m^{-1}\,K^{-1}$
T_0	Room temperature	273 K
f_{ave}	Average solid fraction in droplet	0.75
K_m	Thermal conductivity of metal	40.0 $W\,m^{-1}\,K^{-1}$
ρ_s	Density of metal	6810 $kg\,m^{-3}$
C_{pm}	Specific heat of metal	620 $W\,m^{-1}\,K^{-1}$

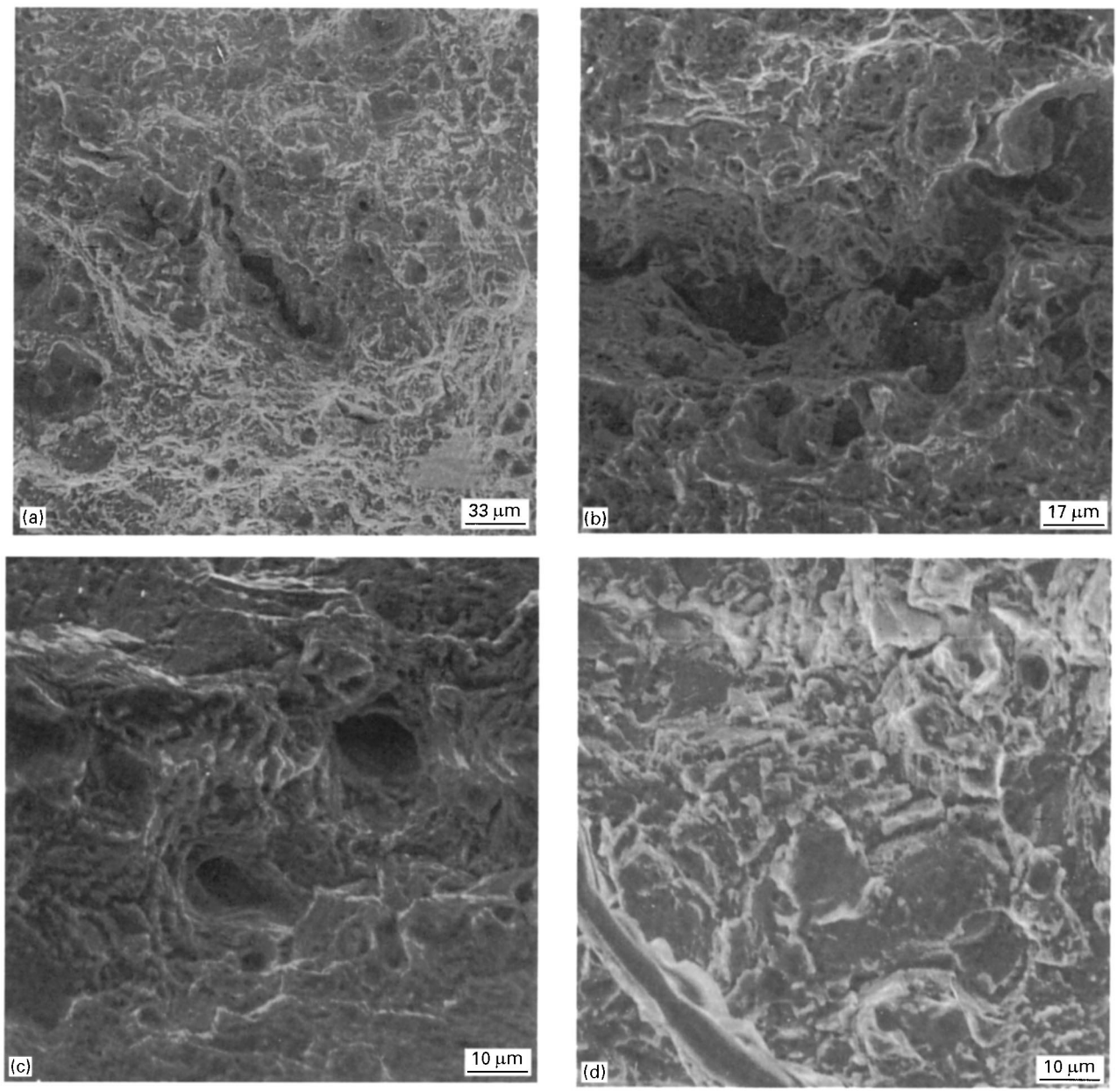

Figure 11 Scanning electron micrographs of the tensile fracture surface of the intermetallic IC-396 showing (a) overall morphology, (b) macroscopic cracks, (c) voids on transgranular surface and (d) fine microscopic cracks.

in the formation of thick prior-droplet boundaries that remain unchanged during subsequent annealing. The elevated mass density associated with the centre of the spray promotes a high degree of compaction, leading to the formation of thin prior-droplet boundaries as observed experimentally. Furthermore, the elevated temperature anneal experienced in this region (Fig. 5b) facilitates the growth and coalescence of the

dendrite fragments, resulting thereby in the formation of a spheroidal grain morphology by the mechanisms that have been previously described. Also, the material at and near the exterior regions is exposed to a similar thermal history as that present in regions with fully developed spheroidal grains, differing only in the rate of heat extraction, which was higher in this region as a direct result of its proximity to the water-cooled substrate. Consequently, the material present in the exterior regions exhibited a heterogeneous grain morphology with associated prior-droplet boundaries.

4.3. Tensile fracture

The tensile fracture surfaces help to provide useful information on processing and microstructural effects on tensile ductility and fracture properties of the polycrystalline intermetallic. Examination of the tensile fracture surface features was carried out in a scanning electron microscope at a low magnification to identify the overall fracture morphology, and at higher magnifications to identify the fine-scale fracture features, providing insight into the fracture mechanics of the materials systems studied. Representative fracture features of the two alloys are shown in Figs 11–15. Fracture of the intermetallic IC-396 was predominantly transgranular, tearing with very little evidence of intergranular failure. The isolated macroscopic and microscopic voids were found on the transgranular fracture surface (Fig. 11c). Gross yielding preceded stable fracture. The suppression of grain-boundary fracture in this boron-containing material results in the intervention of a higher-energy absorbing fracture mode, i.e. ductile transgranular rupture. The increase in grain-boundary strength resulting from the presence of boron increases the resistance to intergranular fracture sufficiently to promote fracture by a higher-energy-absorbing mode. Shallow dimples

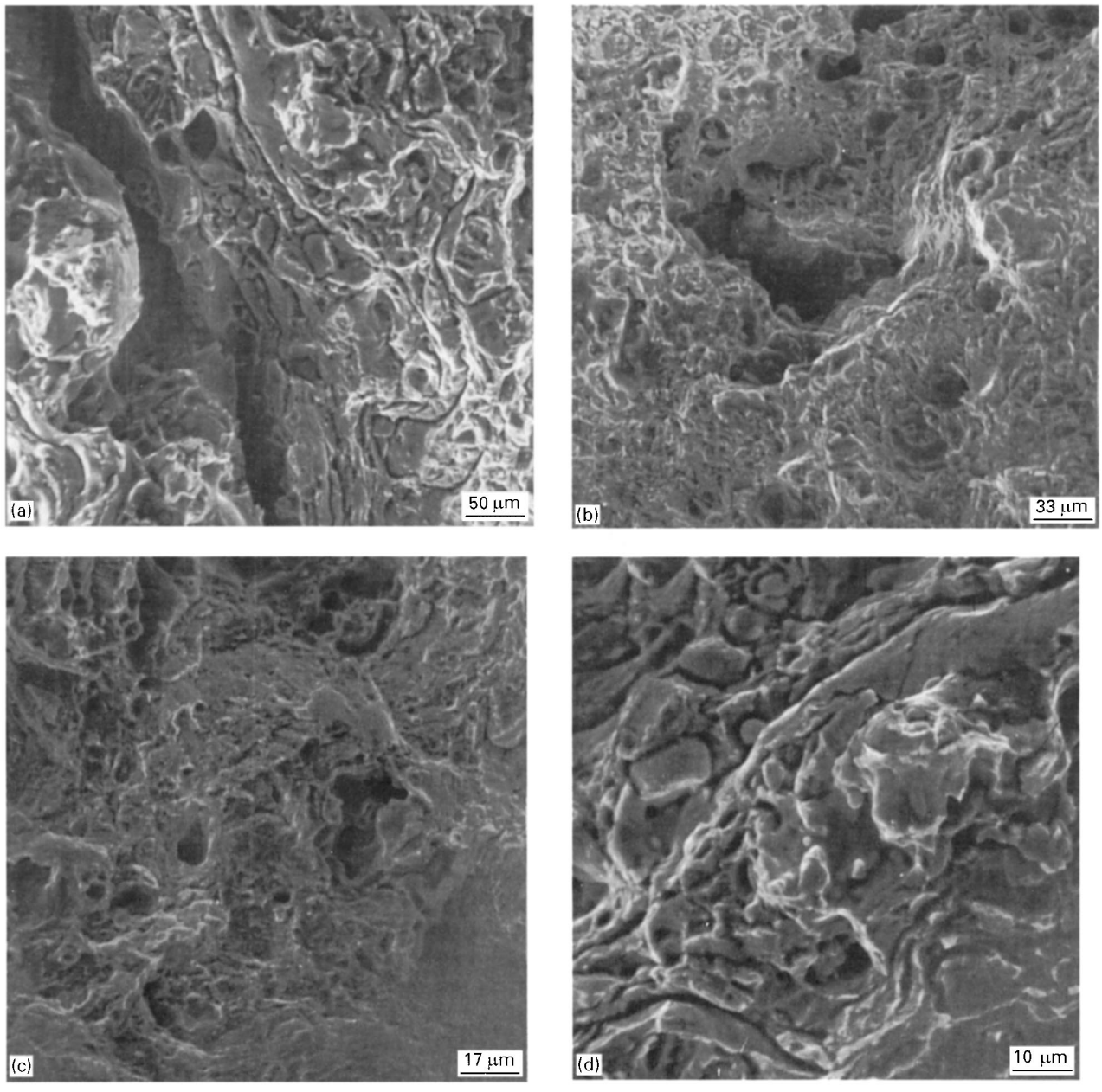

Figure 12 Scanning electron micrographs of the tensile fracture surface of the intermetallic IC-50 showing (a) overall morphology, (b) macroscopic cracks, (c) voids on transgranular surface and (d) fine microscopic cracks.

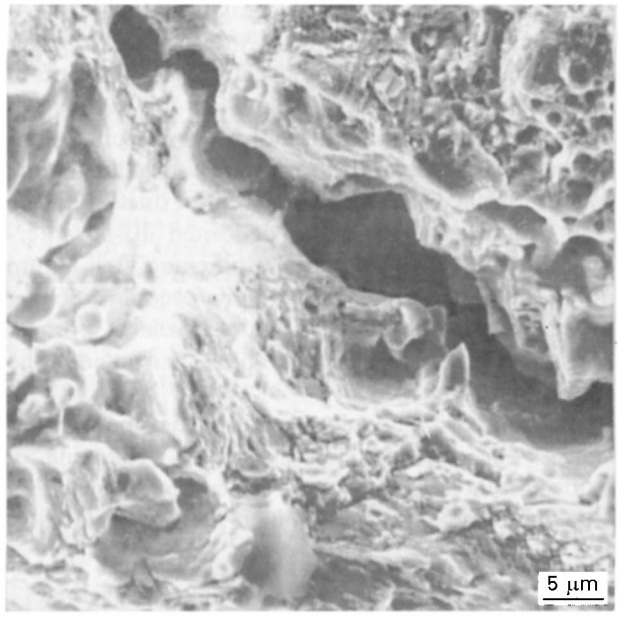

Figure 13 Scanning electron micrograph showing macroscopic crack on the tensile fracture surface of the intermetallic IC-50.

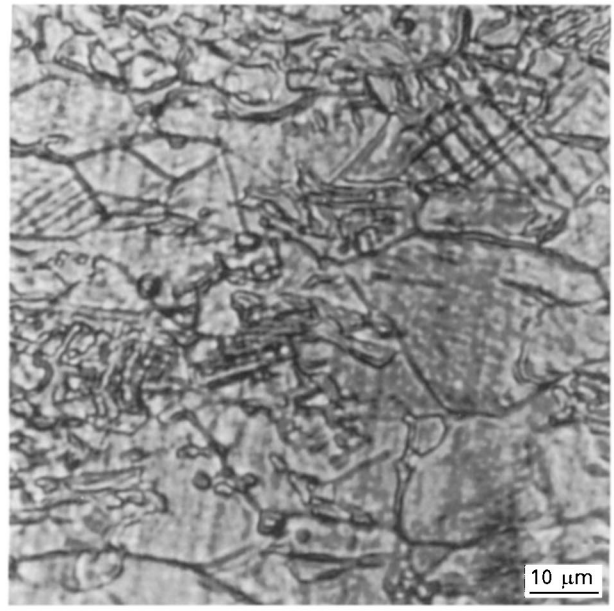

Figure 15 Optical micrograph of a deformed test specimen of the Ni_3Al intermetallic showing deformation bands.

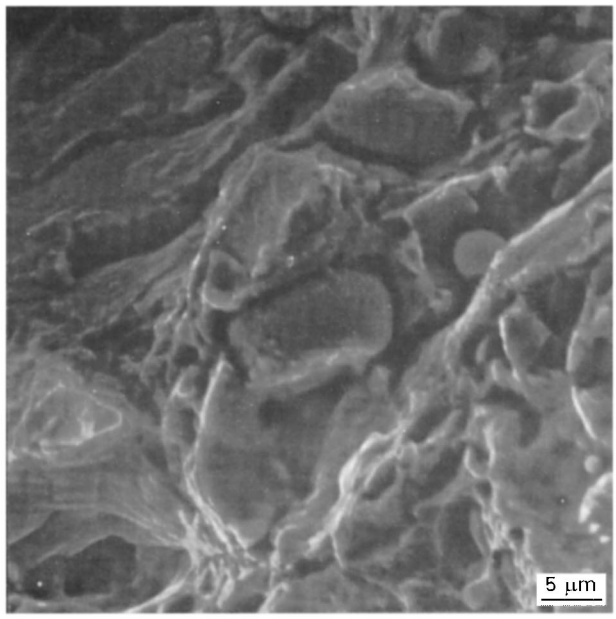

Figure 14 Scanning electron micrograph of the tensile fracture surface of the intermetallic IC-50 showing microscopic cracking around the particles.

were found distributed on the transgranular fracture surface, adjacent to the macroscopic and microscopic voids (Fig. 11c). The existence of pockets of microvoids provides convincing evidence that their formation and presence results from spray deposition processing. Very fine microscopic cracks were observed on the transgranular fracture surface (Fig. 11d).

Fracture surfaces of the intermetallic IC-50 exhibited intergranular cracking, failure along the prior-particle boundaries and traces of transgranular tearing. Macroscopic and numerous microscopic cracks (Fig. 12a) and failure of prior-particle boundaries (Fig. 13) were evident. Macroscopic voids (Fig. 12b) were found intermingled with pockets of microscopic voids (Fig. 12c) and microscopic cracks, indicative of traces of ductile rupture. Isolated pockets of shallow dimples were found adjacent to the voids and covering the transgranular fracture regions.

In an earlier study [61], polycrystalline nickel aluminide (Ni_3Al) was found to be brittle and the alloy failed intergranularly, displaying limited ductility. However, intrinsic microstructural changes and compositional modifications, such as controlled microalloying with boron, and the use of novel processing and synthesis techniques have resulted in an intermetallic compound displaying a higher-energy-absorbing fracture mode. Boron segregates to grain boundaries of the polycrystalline intermetallic compound [62]. The effect of boron appears to be one of strengthening the grain boundaries owing to an increase in the force of interatomic bonds so that they can withstand the stresses arising from deformation. Boron also assists in accommodating the localized plastic deformation by means of generation of lattice dislocations. For this polycrystalline Ni_3Al intermetallic, a far-field stress permits stress concentrations to occur at and along the grain boundaries as well as at the point of intersection of the planar deformation bands with the grain-boundary regions (Fig. 15). Additionally, the transmission electron micrograph in Fig. 16 shows the boron inclusions at the grain boundaries as well as the dislocations piled up at the grain boundaries which result from the accommodation of plastic deformation of the sample. When the concentrated stress at the grain boundary exceeds the cohesive strength of the boundary, intergranular fracture occurs. Therefore, for this Ni_3Al intermetallic material a progressive increase in far-field stress accelerates the intergranular fracture and limits the strain to failure in uniaxial tension.

Planar slip deformation is characteristic of ordered alloys wherein the superlattice dislocations

Figure 16 Transmission electron micrograph on the Ni_3Al intermetallic showing boron inclusions at the grain boundaries and dislocation pile-up at the grain boundaries.

can be visualized as two unit dislocations that move together, resulting in the creation of antiphase boundaries [63]. This dislocation structure restricts cross-slip and, consequently, there exists less likelihood to accommodate slip processes at the grain boundary as dislocations progressively pile up. This explains the increased intergranular cracking (Fig. 13) observed for the polycrystalline intermetallic IC-50 compared with the predominantly transgranular cracking of the IC-396 alloy. Failure along prior particle boundaries (Fig. 14) suggests the interactive influences of weakening by oxide present from the powder process, and concurrent cracking of the initially solidified powder particle.

5. Conclusions

Based on a study of the microstructure and resultant fracture behaviour of spray-atomized and deposited intermetallics, the following are the main conclusions.

1. The microstructure of the intermetallics at and near the substrate consisted of small droplets that arrived on the substrate fully solidified and were enveloped by larger droplets already on the substrate which contained some liquid. The high heat extraction rate associated with the substrate area "froze" the small fully solidified droplets inside the larger droplets containing the fragmented dendrites resulting in the formation of thick prior-droplet boundaries.

2. The elevated mass density at the centre of the spray promotes a high degree of compaction, favouring the formation of thin prior-droplet boundaries. The elevated-temperature anneal facilitates the growth and coalescence of dendrite fragments, resulting in the formation of spheroidal grains.

3. Tensile fracture of the spray-deposited IC-396 intermetallic was predominantly transgranular with little evidence of intergranular failure. Suppression of grain-boundary failure resulted in higher-energy-absorbing transgranular fracture. Macroscopic and microscopic voids and dimples were evident on the fracture surface features reminiscent of ductile failure.

4. Fracture of the spray-deposited IC-50 intermetallic exhibited intergranular cracking with failure along the grain boundaries and microscopic cracking along the prior-particle boundaries. Isolated pockets of shallow dimples were found to be distributed in the transgranular regions.

5. Observed failure along prior-particle boundaries suggest the interactive influences of weakening of oxide present from the powder process and concurrent cracking of the initially solidified powder particles.

Acknowledgements

D. Lawrynowicz, X. Liang and Professor Enrique J. Laverna gratefully acknowledge the support of the Air Force Office of Scientific Research under Grants AASERT F49620-92-J-0262, and F49620-94-1-0137 (Program Manager Dr C. Ward). Dr Srivatsan acknowledges with thanks the State of Ohio: Board of Regents (Grants 5-34021 and 5-34026) for partial support of this research study. The authors thank Ms Pam Hoover for her terminal assistance with the formatting of this manuscript to specifications.

References

1. M. H. YOO, J. H. HORTON and C. T. LIU, *Acta Metall.* **36** (1988) 2935.
2. C. T. LIU and V. K. SIKKA, *J. Metals* **38** (1986) 19.
3. *Idem., ibid.* (1993) 38.
4. N. S. STOLOFF (ed.), "High temperature ordered intermetallic alloys II", Materials Research Society Symposium Proceedings, Vol. 81 (Materials Research Society, Pittsburgh, PA, 1987).
5. C. T. LIU (ed.), "High temperature ordered intermetallic alloys III", Materials Research Society Symposium Proceedings, Vol. 133 (Materials Research Society, Pittsburgh, PA, 1989).
6. L. A. JOHNSON, D. P. POPE and J. O. STIEGLER (eds), "High temperature ordered intermetallic alloys IV", Materials Research Society Symposium Proceedings, Vol. 213 (Materials Research Society, Pittsburgh, PA, 1991).
7. E. A. AITKEN, "Intermetallic compounds" (Wiley–Interscience, New York, 1967) pp. 491–495.
8. E. M. GRALA, "Mechanical properties of intermetallic composites" (Wiley–Interscience, New York, 1969) pp. 358–368.
9. R. MOSKOVICH, *J. Mater. Sci.* **13** (1978) 1901.
10. A. V. SEYBOLT and J. H. WESTBROOK, *Acta Metall.* **12** (1967) 449.
11. K. AOKI and O. IZUMI, *Trans. Jpn Inst. Metals* **19** (1978) 203.
12. G. W. GROVES and A. KELLY, *Phil. Mag.* **8** (1963) 877.
13. S. V. RAJ, R. D. NOEBE and R. BOWMAN, *Scripta Metall.* **23** (1989) 2049.
14. C. T. LIU, C. L. WHITE and J. A. HORTON, *Acta Metall.* **33** (1985) 213.
15. C. T. LIU and C. L. WHITE, *ibid.* **35** (1987) 643.
16. C. T. LIU, "High temperature ordered intermetallic alloys II", Materials Research Society Symposium Proceedings, Vol. 81, edited by N. S. Stoloff (Materials Research Society, Pittsburgh, PA, 1987) pp. 355–365.
17. N. S. STOLOFF, *Int. Mater. Rev.* **34** (1989) 153.
18. K. AOKI, *Mater. Trans. Jpn Inst. Metals* **31** (1990) 443.

19. A. I. TAUB, S. C. HUANG and K. M. CHANG, *Metall. Trans. A* **15** (1984) 399.
20. A. I. TAUB, K. M. CHANG and C. T. LIU, *Scripta Metall.* **20** (1986) 1613.
21. I. M. BAKER, E. M. SCHULSON and J. A. HORTON, *Acta Metall.* **35** (1987) 1533.
22. J. J. LEWANDOWSKI, C. A. HIPPSLEY, M. B. D. EFFIS and J. F. KNOTT, *ibid.* **35** (1987) 593.
23. P. S. KHADKIKAR, J. J. LEWANDOWSKI and K. VEDULA, *Metall. Trans. A* **20** (1989) 1247.
24. M. S. KIM, S. HANADA, S. WATANABE and O. IZUMI, *J. Mater. Sci.* **25** (1990) 1590.
25. C. L. WHITE, R. A. PADGETT, C. T. LIU and S. M. YALISOVE, *Scripta Metall.* **18** (1984) 1417.
26. A. CHOUDHURY, C. L. WHITE and C. R. BROOKS, *ibid.* **20** (1986) 1061.
27. A. R. E. SINGER, *Metal Powder Rep.* **41** (1986) 117.
28. E. J. LAVERNIA, *Int. J. Rapid Solidification* **5** (1989) 47.
29. P. MATHUR and A. LAWLEY, *J. Metals* **41** (1989) 23.
30. E. J. LAVERNIA, J. D. AYERS and T. S. SRIVATSAN, *Int. Mater. Rev.* **37** (1992) 1.
31. T. S. SRIVATSAN and E. J. LAVERNIA, in "Processing and frabrication of advanced materials for high temperature applications II", edited by V. A. Ravi and T. S. Srivatsan (The Minerals, Metals and Materials Society, Warrendale, PA, 1993).
32. X. LIANG and E. J. LAVERNIA, *Mater. Sci. Eng.* (1995) in press.
33. M. GUPTA, F. A. MOHAMED and E. J. LAVERNIA, *Metall. Trans. A* **23** (1992) 831.
34. Y. WU and E. J. LAVERNIA, *J. Metals* **43** (1991) 32.
35. M. GUPTA, F. A. MOHAMED and E. J. LAVERNIA, *Mater. Sci. Eng. A* **144** (1991) 99.
36. R. MEHRABIAN, *Int. Metal Rev.* **24** (1982) 186.
37. P. MATHUR, D. APELIAN and A. LAWLEY, *Acta Metall.* **37** (1989) 429.
38. E. M. GUTIERREZ, E. J. LAVERNIA, G. M. TRAPAGA, J. SZEKELY and N. J. GRANT, *Metall. Trans. A* **20** (1989) 71.
39. M. GUPTA, F. A. MOHAMED and E. J. LAVERNIA, *Int. J. Rapid Solidification* **6** (1991) 247.
40. X. LIANG and E. J. LAVERNIA, *Mater. Sci. Eng. A* **153** (1992) 646.
41. X. LIANG, J. EARTHMAN and E. J. LAVERNIA, *Acta Metall.* **40** (1992) 3003.
42. X. LIANG, H. K. KIM, J. C. EARTHMAN and E. J. LAVERNIA, *Mater. Sci. Eng. A* **153** (1992) 654.
43. M. GUPTA, T. S. SRIVATSAN, F. A. MOHAMED and E. J. LAVERNIA, *J. Mater. Sci.* **28** (1993) 2245.
44. S. PING YAN, F. A. MOHAMED, T. S. SRIVATSAN and E. J. LAVERNIA, *ibid.* **29** (1994) in press.
45. C. T. LIU and V. K. SIKKA, *J. Metals* **38** (1986) 19.
46. R. N. WRIGHT and V. K. SIKKA, *J. Mater. Sci.* (1988) 4315.
47. "Standard method for sieve analysis of granular metal powders", ASTM Standard B214-92 (American Society for Testing and Materials, Philadelphia, PA, 1992).
48. J. FUKAI, Z. ZHAO, D. POULIKAKOS, C. M. MEGARIDIS and O. MIYATAKE, *Phys. Fluids A* **5** (1993) 2588.
49. J. MADEJSKI, *Int. J. Heat Mass Transfer* **19** (1976) 1009.
50. C. SAN MARCHI, H. LIU, E. J. LAVERNIA, R. H. RANGEL, A. SICKINGER and E. MUEHLBERGER, *J. Mater. Sci.* **28** (1993) 3313.
51. H. LIU, E. J. LAVERNIA and R. H. RANGEL, *Atomization Sprays* **4** (1994) 369.
52. *Idem., Acta Metall. Mater.* **43** (1995) 2053.
53. *Idem., J. Phys. D: Appl. Phys.* **26** (1993) 1900.
54. *Idem., Acta Metall. Mater.* **43** (1995) 2053.
55. J. M. HILL, "One-dimensional Stefan problems: an introduction" (Longman Scientific and Technical, Wiley, New York, 1987).
56. T. WATANABE, I. KURIBAYASHI, T. HONDA and A. KANZAWA, *Chem. Eng. Sci.* **47** (1992) 3059.
57. P. S. GRANT and B. CANTOR, *Acta Metall. Mater.* **43** (1995) 913.
58. G. TRAPAGA and J. SZEKELY, *Metall. Trans. B* **22** (1991) 901.
59. A. ANNAVARAPU, D. APELIAN and A. LAWLEY, *Metall. Trans. A* **21** (1990) 3237.
60. X. LIANG, J. C. EARTHMAN, J. WOLFENSTINE and E. J. LAVERNIA, *Mater. Charact.* **28** (1992) 173.
61. R. W. GUARD and J. H. WESTBROOK, *Trans. Metall. Soc. AIME* **215** (1959) 807.
62. C. T. LIU, C. C. WHITE, C. C. KOCH and E. H. LEE, in "High temperature materials chemistry II", Vol. 83, edited by Z. A. Munir and D. Cubicciotti (1983) pp. 32–42.
63. J. R. RIGNEY and J. J. LEWANDOWSKI, *Mater. Sci. Eng. A* **149** (1992) 143.

Received 10 October 1995
and accepted 20 January 1997